Supporting Information

In-Situ Dipole Formation to Achieve High Open-Circuit Voltage in Inverted Perovskite Solar Cells via Fluorinated Pseudohalide Engineering

*Yuan Liu, Chen Tang, Anxin Sun, Rongshan Zhuang, Yiting Zheng, Congcong Tian, Xueyun Wu, Zihao Li, Beilin Ouyang, Jiajun Du, Ziyi Li, Yong Hua, Chun-Chao Chen**

Y. Liu, C. Tang, A. Sun, Y. Zheng, C. Tian, X. Wu, Z. Li, B. Ouyang, J. Du, Z. Li, Prof. C. Chen

School of Materials Science and Engineering

Shanghai Jiao Tong University

Shanghai 200240, P. R. China

E-mail: c3chen@sjtu.edu.cn

R. Zhuang, Prof. Y. Hua

Yunnan Key Laboratory for Micro/Nano Materials & Technology

School of Materials and Energy

Yunnan University

Kunming 650091, P. R. China

Keywords: Fluorinated pseudohalide engineering, nonradiative recombination, cascade energy-level arrangement, excitonic binding energy, inverted perovskite solar cells.

Experimental Section

Materials:

N,N Dimethylformamide (DMF, 99.8%), Dimethyl sulfoxide (DMSO, 99.8%), Isopropanol (IPA, 99.5%) and Anisole (Ani, 99.9%) are purchased from Sigma Aldrich Chemical Co., Ltd. Methanol (MeOH, >99.9%) is gained from Aladdin Reagent (Shanghai) Co., Ltd. Formamidine iodide (FAI, >99.5%) is purchased from Greatcell Solar Materials Pty Ltd. Lead (II) iodide (PbI_2, >99.99%) and bathocuproine (BCP) are purchased form Xi'an E-Light New Material Co., Ltd. Cesium iodide (CsI, >99.99%), methylammonium bromide (MABr, >99.5%), and [4-(3,6-Dimethoxy-9H-carbazol-9-yl)ethyl] phosphonic acid (MeO-4Pacz) are purchased from Xi'an Polymer Light Technology Crop. [6,6]-Phenyl-C61-butyric acid methyl ester (PCBM) is purchased from Lumtec, Taiwan. 3-(aminomethyl) piperidinium iodide (3AMP) is purchased from Shanghai MaterWin New Materials Co., Ltd. All materials used directly after purchase without further processing.

Device fabrication:

The FTO substrates are washed in ultrasonic bath with deionized water, detergent, anhydrous ethanol, acetone and isopropyl alcohol successively for 15 min. Before use, the FTO substrates are blown dry and treated with UV-Ozone for 20 min. Then, the FTO substrates are transferred into the nitrogen-filled glovebox quickly. After that, MeO-

4Pacz (0.1 mM in MeOH) solution is spin-coated on FTO substrates at 3000 rpm for 30 s, and annealed at 100 ℃ for 10 min. The perovskite layer is spin-coated on the substrate by one-step deposition method. The perovskite precursor solution of 1.4 M $Cs_{0.05}(FA_{0.92}MA_{0.08})_{0.95}Pb(I_{0.92}Br_{0.08})_3$ is prepared by dissolving FAI, CsI, PbI_2, $PbBr_2$ and MABr in DMF/DMSO (4:1, *v*/*v*) mixed solvent according to stoichiometric formula. EMIMTFSI, EMIMFSI and EMIMDCA are added into the precursor solution in molar ratio (0.2/0.5/0.7/1/2%). The perovskite precursor solution is thoroughly stirred at room temperature for more than 24 h and filtered through a polytetrafluoroethylene (PTFE) filter (0.22 μm) before use. Then, 60 μL perovskite precursor solution is dropped onto FTO/MeO-4Pacz substrates, spin-coated at 1000rpm for 25 s and 5000 rpm for 30 s. The 120 μL of Anisole is poured on the substrates 7 s prior to the end of the program and then the substrates are annealed at 100 °C for 15 min. For post-processing, 3AMP (3mM in IPA) solution is spin-coated on annealed perovskite films at 5000 rpm for 30 s, and annealed at 100 ℃ for 10 min. Then, PCBM (20 mg/ml in CB) is spin-coated at 2000 rpm for 30 s and BCP is spin-coated at 5000 rpm for 30 s. Finally, Ag (100 nm) is deposited as back electrode through a mask by thermal evaporation under 9.9×10^{-5} Pa. And the effective area of the electrode is 0.062 cm^2.

Calculating Section

ESP Calculating Methods:

Gaussian 09 program is used to calculate the ESP and dipole moment of DCA^-, FSI^-, $TFSI^-$ and $EMIM^+$. Their geometry optimizations are conducted by using B3LYP functional[1] and the all-electron double-ξ valence basis sets of 6-31G*.[2] Vibrational frequency calculations are also used to ensure that the optimized structure has no imaginary frequency.

DFT Calculating Methods:

All the calculations are performed in the framework of the density functional theory with the projector augmented plane-wave method, as implemented in the Vienna ab initio simulation package.[3] The generalzied gradient approximation proposed by Perdew, Burke, and Ernzerhof is selected for the exchange-correlation potential.[4] The cut-off energy for plane wave is set to 500 eV. The energy criterion is set to 10^{-5} eV in iterative solution of the Kohn-Sham equation. The Brillouin zone integration is performed using a 2×3×1 k-mesh. All the structures are relaxed until the residual forces on the atoms have declined to less than -0.02 eV/Å. Finally, the adsorption energies (E_{ads}) are calculated as $E_{ads}=E_{ad/sub}-E_{ad}-E_{sub}$, where $E_{ad/sub}$, E_{ad} and E_{sub} are the optimized adsorbate/substrate system, the adsorbate in the structure and the clean substrate respectively.

Quasi-Fermi level splitting (QFLS) Calculating Methods:

Radiative QFLS ($QFLS_{rad}$) are obtained from the following equation:

$$QFLS_{rad} = k_B T ln\left(\frac{J_G}{J_{rad,0}}\right)$$

where k_B, T, J_G and $J_{rad,0}$ are Boltzmann constant, thermal equilibrium temperature, generation current density, dark radiative saturation current density, respectively. J_G is the integral product of the EQE spectrum, and $J_{rad,0}$ can be determined by the following equation:[5-6]

$$J_{rad,0} = q\int EQE_{PV}(E)\phi_{bb}(E)dE$$

where q is the elementary charge, E is the photo energy, $\phi_{bb}(E)$ is the black body photon flux, which can be determined by the following equation:

$$\phi_{bb}(E) = \frac{2\pi E^2}{(h^3c^2)} exp\left(\frac{-E}{k_B T}\right)$$

Where h the Planck constant and c is the light velocity in vacuum.

Internal QFLS can be calculated based on the relationship with PLQY according to following equation:

$$QFLS = QFLS_{rad} + k_B T ln(PLQY)$$

V_{OC} Loss Calculating Methods:

According to the Shockley-Queisser (S-Q) limit, the total loss of V_{OC} is divided into two parts:[7]

$$E_g = qV_{OC} + q\Delta V_{total} = qV_{OC} + q\Delta V_1 + q\Delta V_2$$

where q is the elementary charge, $q\Delta V_1$ is themodynamic and radiative recombination loss, which can be determined by the following equation:

$$q\Delta V_1 = E_g - qV_{rad} = E_g - QFLS_{rad}$$

$q\Delta V_2$ is non-radiative recombination loss, which can be determined by the following equation:

$$q\Delta V_2 = E_g - q\Delta V_1 - qV_{OC}$$

FF Loss Calculating Methods:

The FF loss between Shockley-Queisser (S-Q) limit value of FF and the FF measurement value consists of non-radiative recombination loss and charge transport loss. The FF maximum value (FF_{max}) without charge transport loss can be determined by the following equation:[8]

$$FF_{max} = \frac{qV_{OC} - nk_BTln(qV_{OC} + 0.72nk_BT) - nk_BTln(nk_BT)}{qV_{OC} + nk_BT}$$

where q is the elementary charge, n is the ideal factor, k_B is Boltzmann constant, T is thermal equilibrium temperature.

Characterization Section

X-ray diffraction (XRD) patterns are taken on a D8 Advance X-ray diffractometer with Cu Ka radiation as the X-ray source with a scan rate of 8º min^{-1}. Grazing incidence wide angle X-ray scattering (GIWAXS) tests are performed at beamline BL14B in the Shanghai Synchrotron Radiation Facility (SSRF) with an X-ray wavelength of 0.124 nm, the GIWAXS patterns are acquired with a grazing incidence angle of 0.3º and an exposure time of 60 s. Time-of-flight secondary ion mass spectra (ToF-SIMS) spectra are detected by ToF SIMS 5-100 (Primary ion beam: Bi^{3+}, 30 keV, incident angle: 45 deg, scanning area: 150×150 um^2, pixel: 128×128, beam current: 0.48 pA). Ultraviolet photoelectron spectroscopy (UPS) is measured by AXIS Ultra DLD machine under excitation from the He I line (21.22 eV) of a helium discharge lamp.

Liquid nuclear magnetic resonance (NMR) spectra are measured on a Bruker AVANCE III HD 400 with DMSO-D6 as the solvent. Fourier transform infrared (FTIR) spectra are recorded using a Thermo-Nicolet iS5 instrument. X-ray photoelectron spectra (XPS) is acquired on an AXIS Ultra DLD X-ray photoelectron spectrometer and calibrated based on the C 1s peak (284.8 eV). And for depth profiling XPS (DP-XPS), the etching rate is 54 nm/layer and the etching time for each layer is about 100 s.

Scanning electron microscopy (SEM) and energy dispersive

spectroscopy (EDS) images are obtained by field emission scanning electron microscopy (JSM-7800F). Atomic force microscope (AFM) and Kelvin probe force microscopy (KPFM) are measured by Bruker Bio-FastScan AFM.

UV-vis absorption spectra are acquired on a Lambda 35 UV-vis spectrometer. Steady state photoluminescence (PL), time-resolved photoluminescence (TRPL) and photoluminescence quantum efficiency (PLQY) are tested using FLS 1000 photoluminescence spectrometer with the excitation wavelength of 470 nm. Drive-level capacitance profiling (DLCP) are performed by using an Agilent E4980A precision LCR meter. The DLCP measurements are conducted in the DC bias scanning from 0 to 1.1 V. While the amplitude of the AC biases is ranging from 20 to 200 mV. The scanning range of the AC frequency is 0.01–1000 kHz. electron spin resonance (ESR) measurements are performed with an X-band ESR spectrometer (JEOL RESONANCE, JES-FA200).

Current density-voltage (*J-V*) curves of the device (area: 0.062 cm^2) are obtained under AM1.5G illumination at 100 mW/cm^2 (calibrated by a standard VLSI Si reference solar cell (SRC-1000-TC-K-QZ)) using an Abet Technologies Sun 2000 solar simulator and a Keithley 2400 source meter. External quantum efficiency (EQE) spectra are tracked by the QTEST HIFINITY 5 EQE system (the light intensity is calibrated with Si detectors) in ambient air. Transient photovoltage (TPV) and transient

photocurrent (TPC) curves are detected by Fluxim Paios Spectrometer. Electrochemical impedance spectroscopy (EIS) spectra and Mott Schottky curve (M-S) are observed on a Chenhua CHI660E electrochemical workstation under dark conditions. The water contact angle images are measured on a DSA100 contact angle analysis instrument.

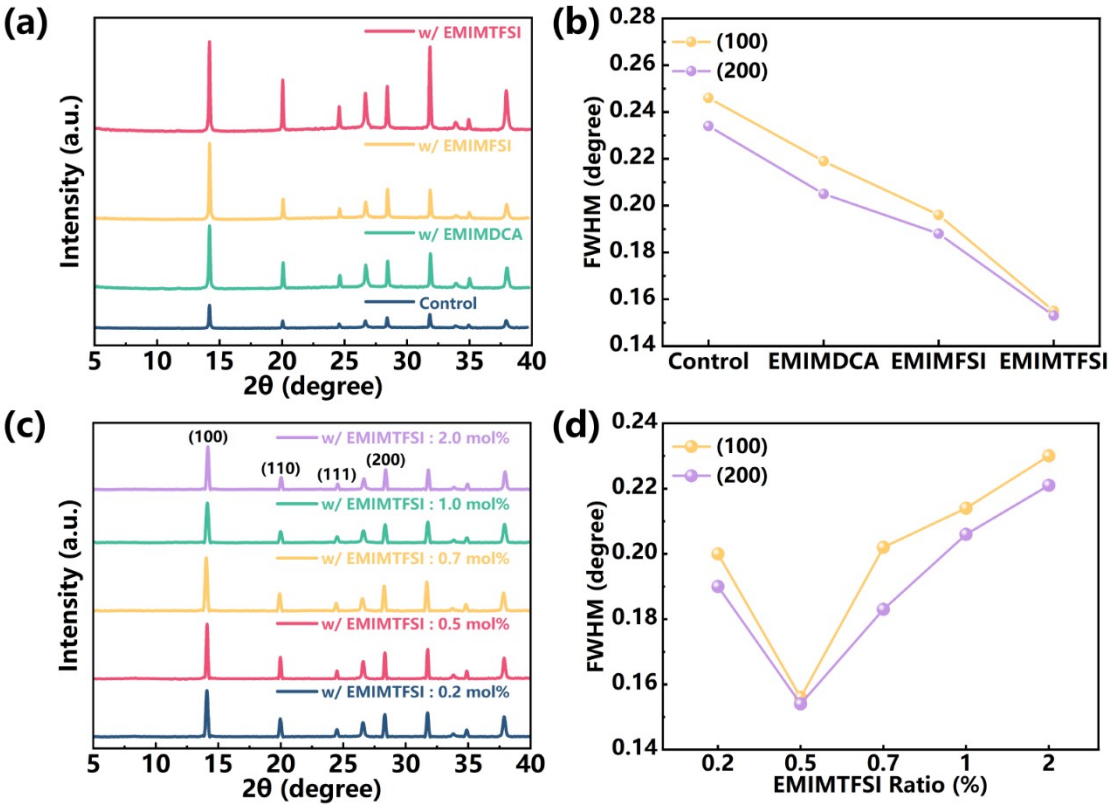

Figure S1. a) XRD patterns and b) the FWHM of the (100) and (200) facet of perovskite films with or without PH-IL optimization. c) XRD patterns and d) the FWHM of the (100) and (200) facet of perovskite films with different addition amount of EMIMTFSI (0.2, 0.5, 0.7, 1, 2%).

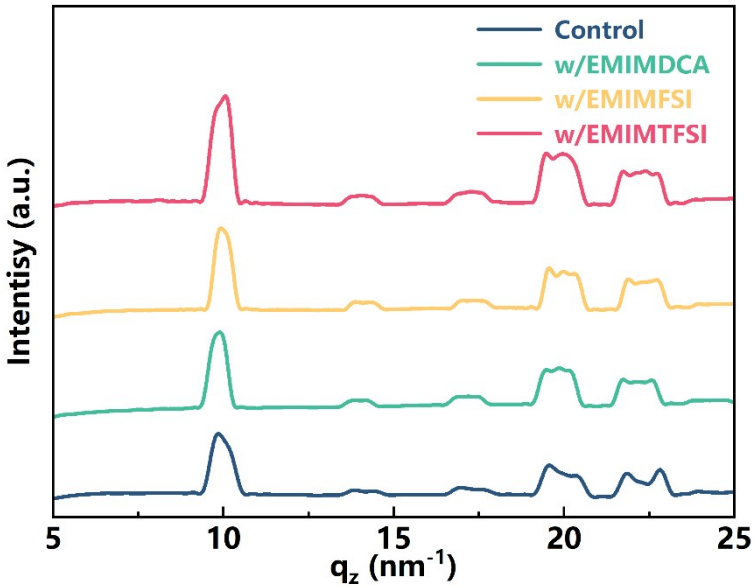

Figure S2. The 1D-GIWAXS profiles along the out-of-plane direction (q_z) of perovskite films with or without PH-IL optimization.

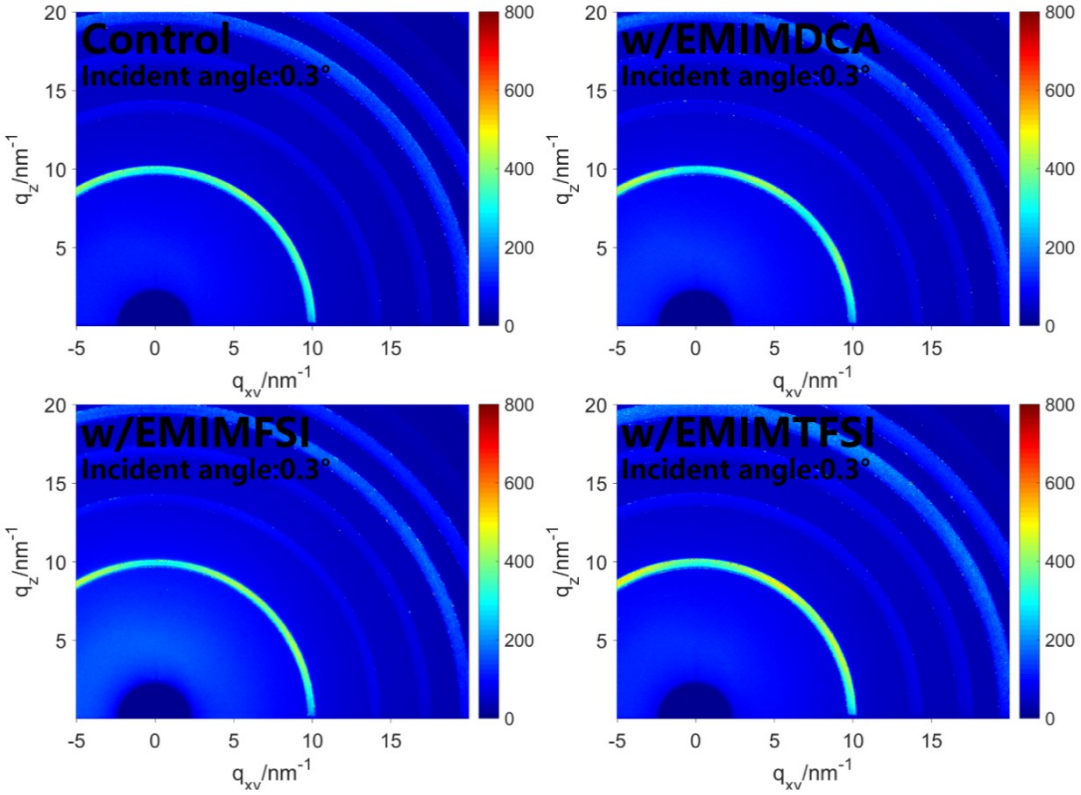

Figure S3. GIWAXS patterns of perovskite films with or without PH-IL optimization (incident angle: 0.3°).

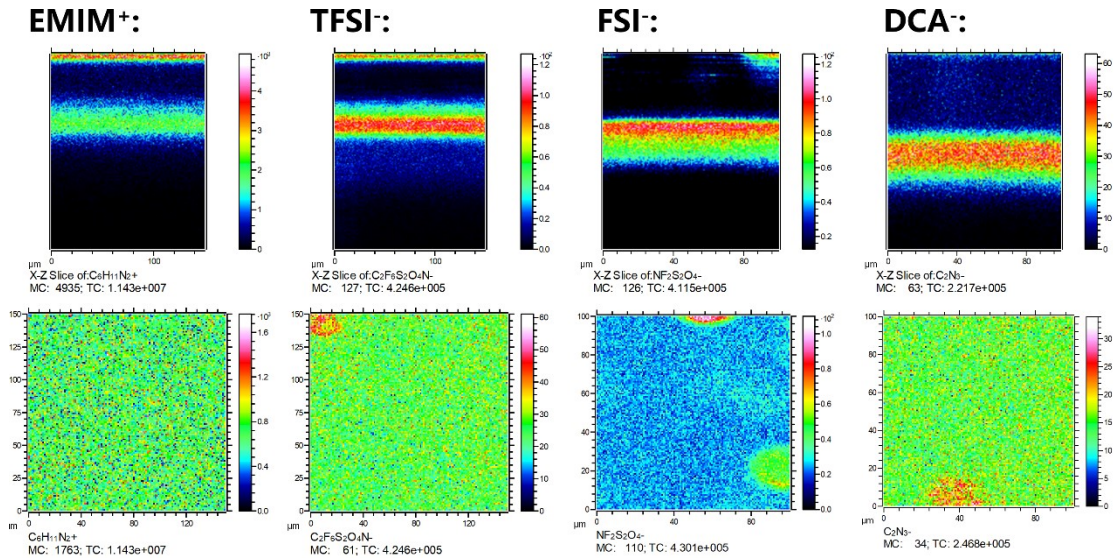

Figure S4. ToF-SIMS side-view and section-view images of $EMIM^+$, $TFSI^-$, FSI^- and DCA^-.

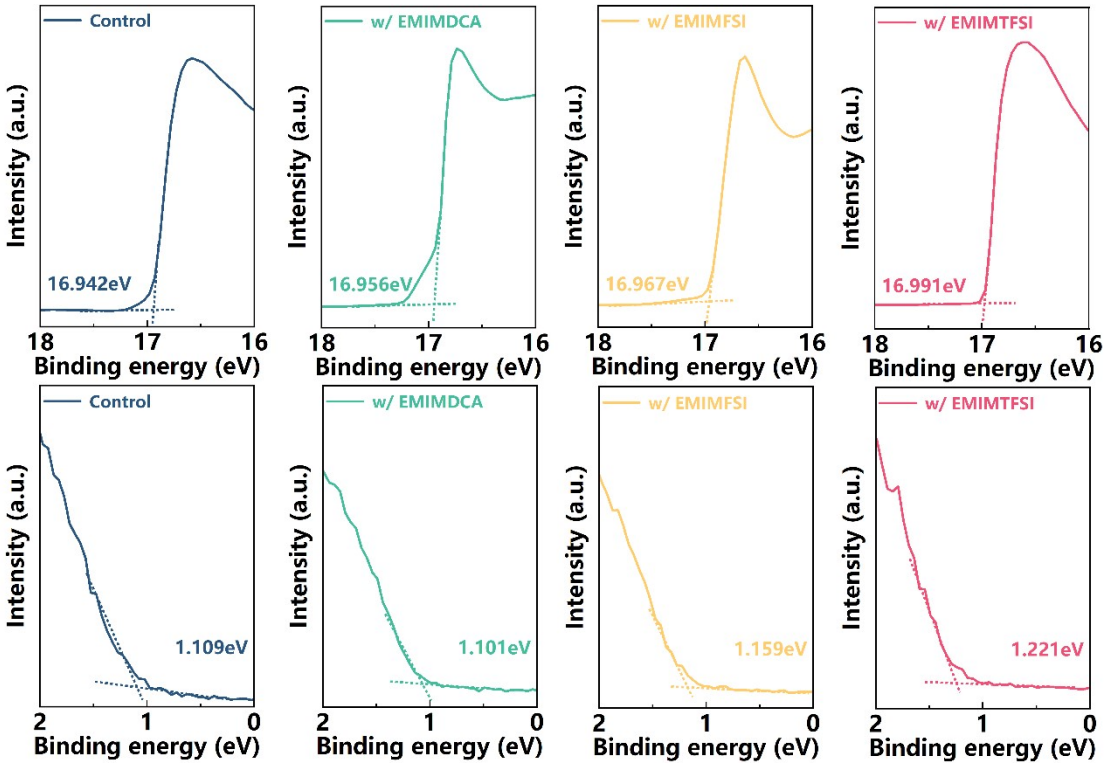

Figure S5. The UPS spectrum of perovskite films with or without PH-IL optimization.

Calculation details:

The work function (WF) can be obtained from the equation as follows: $WF = h\nu - E_{cutoff}$.

The HOMO level can be obtained from the equation as follow: $VBM = -WF - E_{Fermi}$.

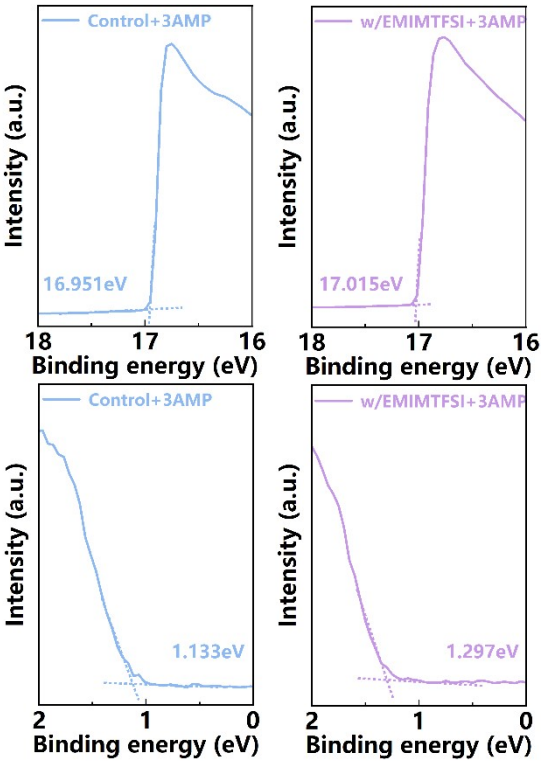

Figure S6. The UPS spectrum of Control+3AMP and w/EMIMTFSI+3AMP.

Calculation details:

The work function (WF) can be obtained from the equation as follows: $WF = h\nu - E_{cutoff}$.

The HOMO level can be obtained from the equation as follow: $VBM = -WF - E_{Fermi}$.

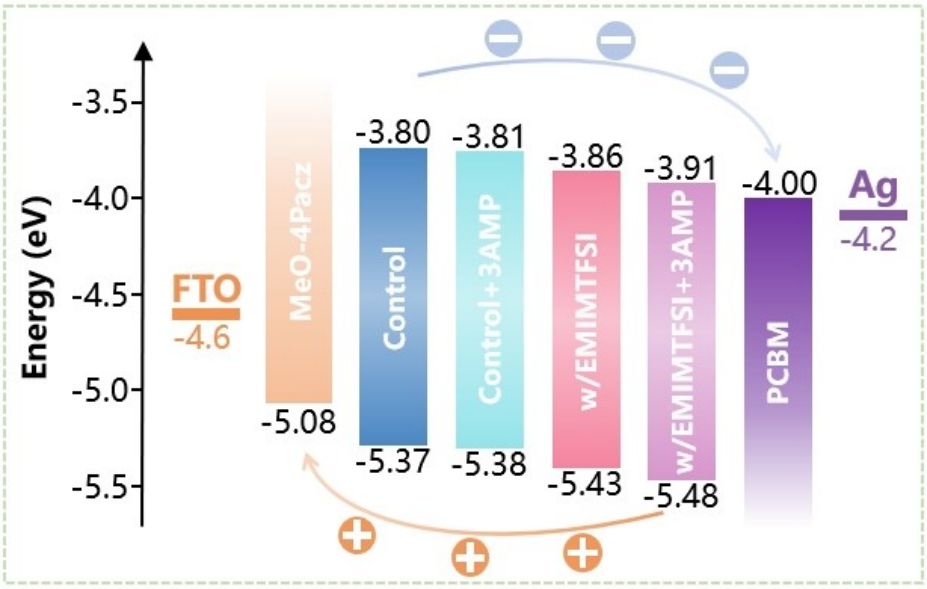

Figure S7. Energy level diagram of every layer in Control, Control+3AMP, w/EMIMTFSI and w/EMIMTFSI+3AMP.

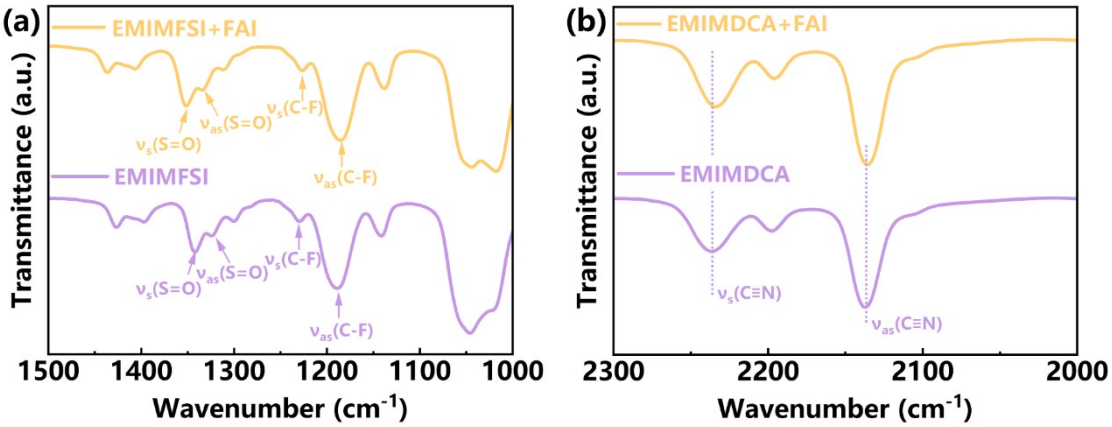

Figure S8. FTIR pattern of a) EMIMFSI and EMIMFSI+FAI, b) EMIMDCA and EMIMDCA+FAI.

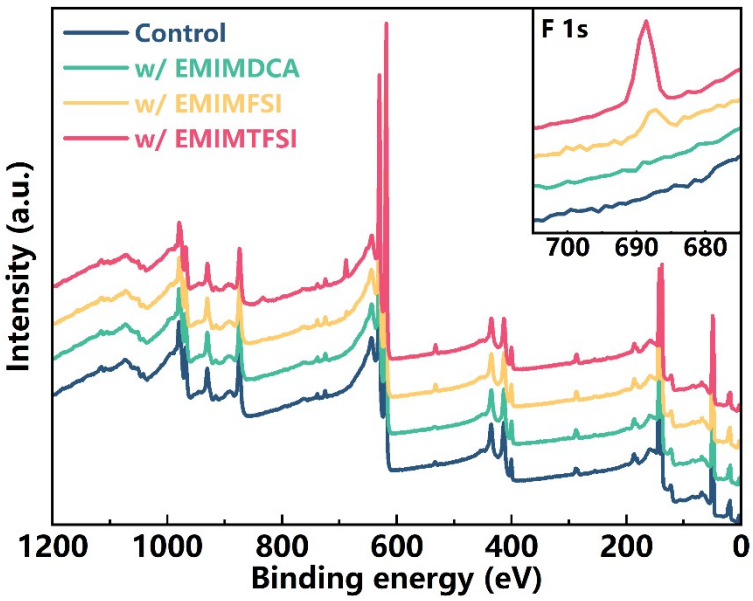

Figure S9. XPS full spectrum and F 1s region of perovskite films with or without PH-IL optimization.

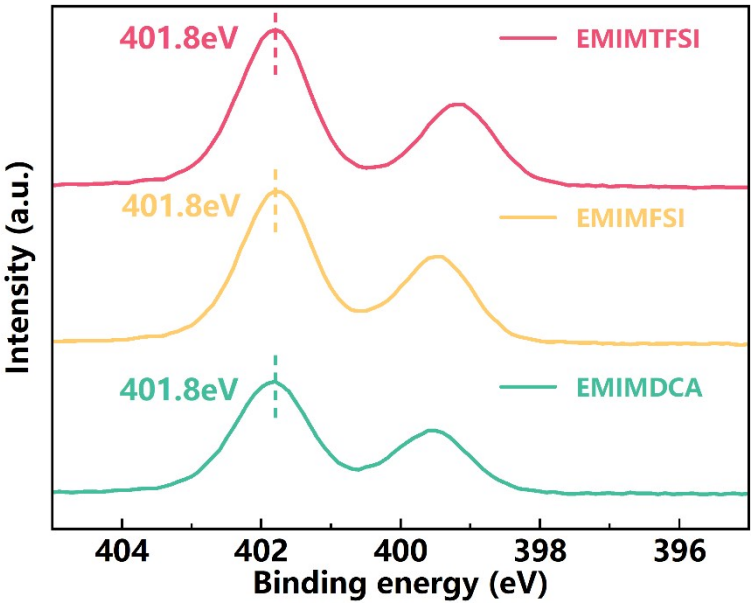

Figure S10. XPS patterns of N 1s in EMIMDCA, EMIMFSI and EMIMTFSI.

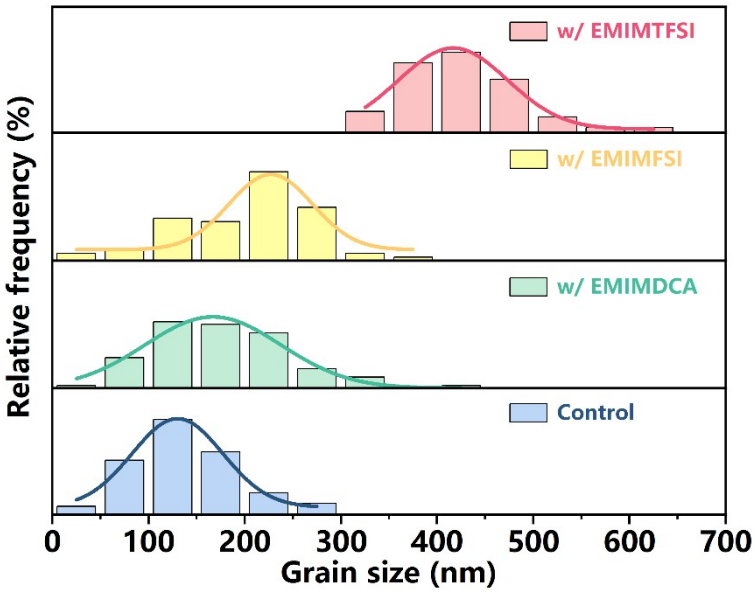

Figure S11. Particle size distribution of SEM images.

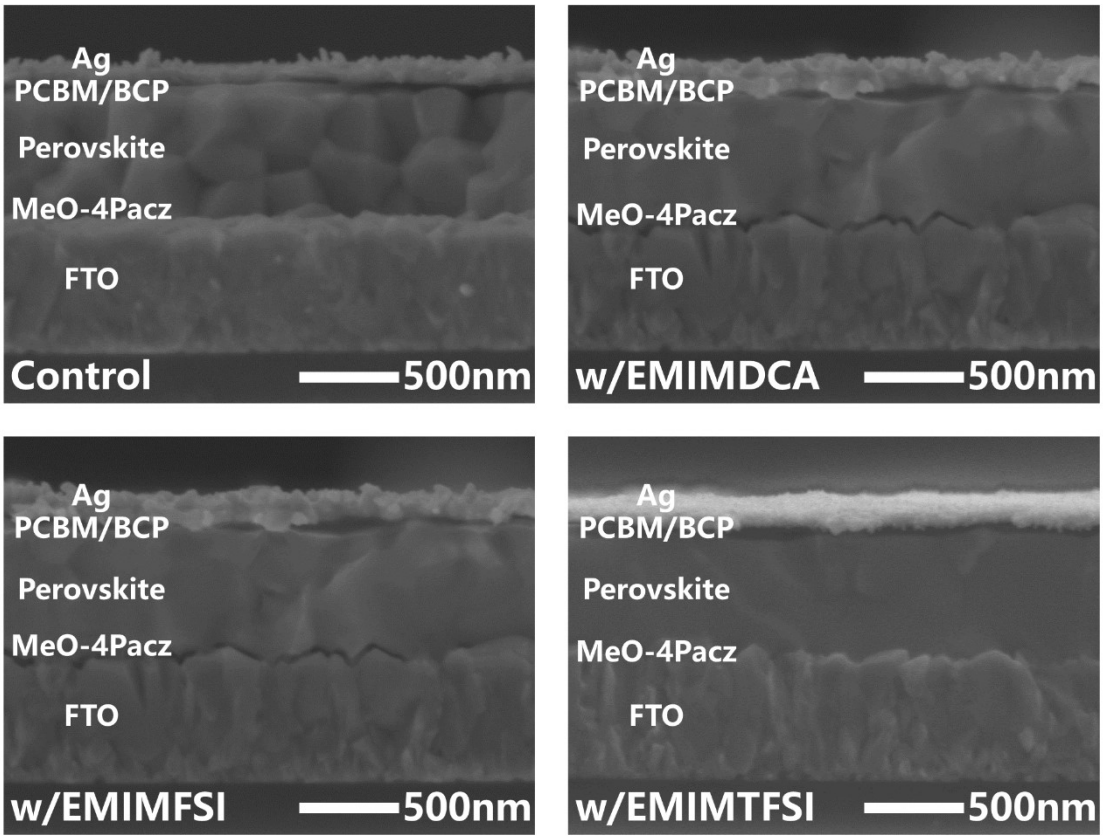

Figure S12. Top-view SEM images of perovskite films with or without PH-IL optimization.

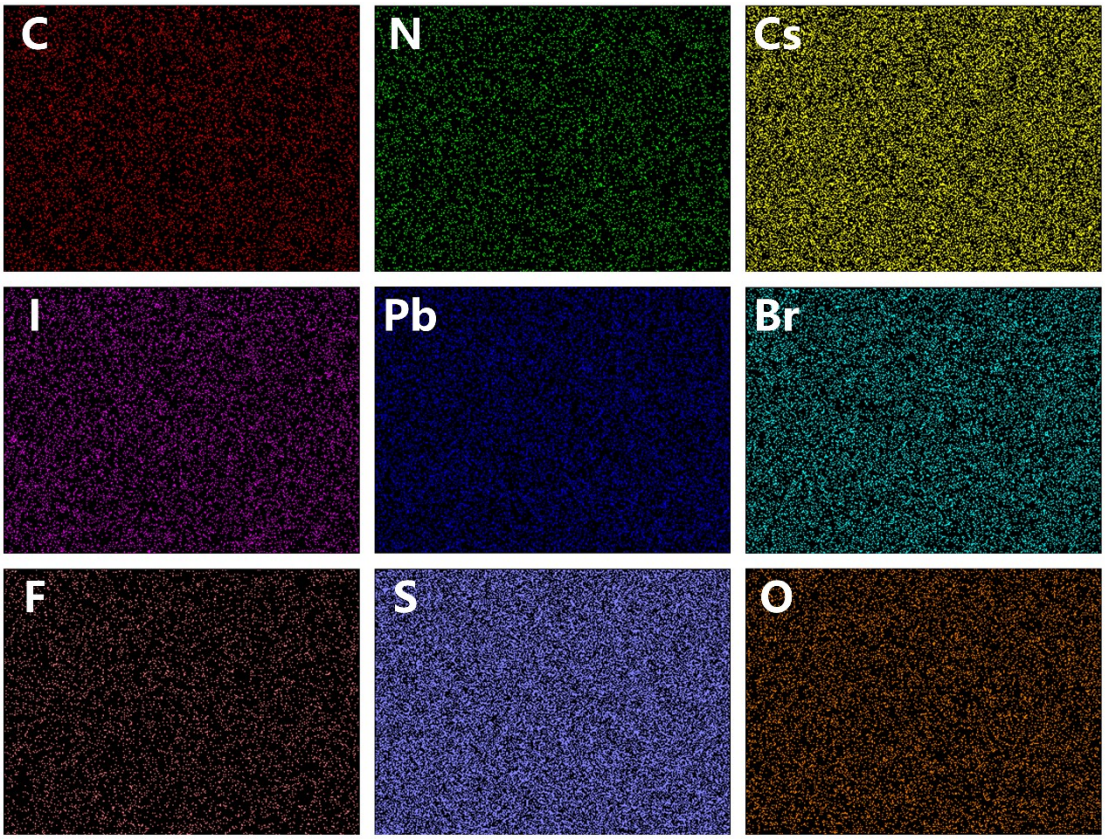

Figure S13. EDS face scan image of w/EMIMTFSI.

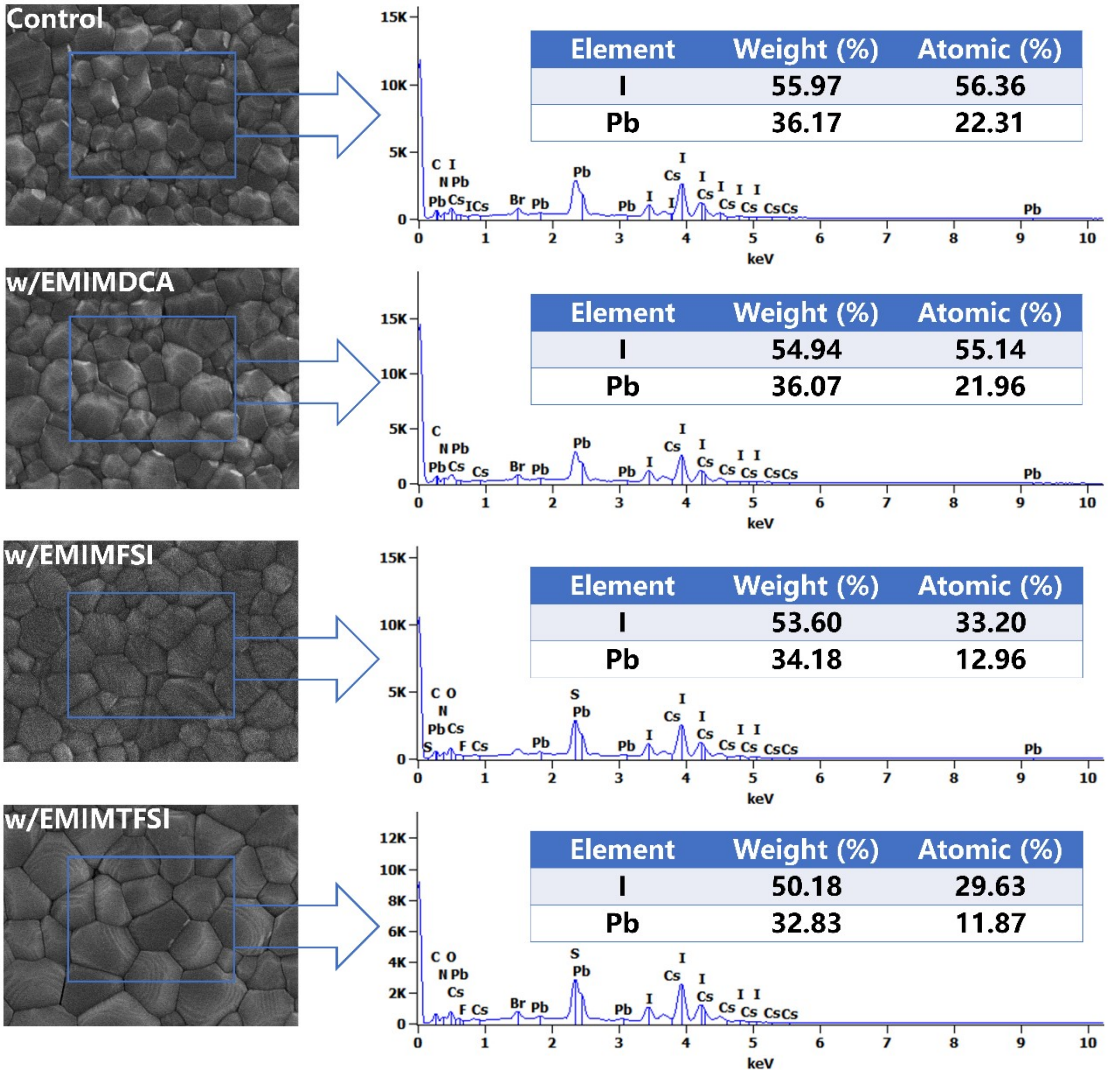

Figure S14. EDS line scan images of perovskite films with or without PH-IL optimization.

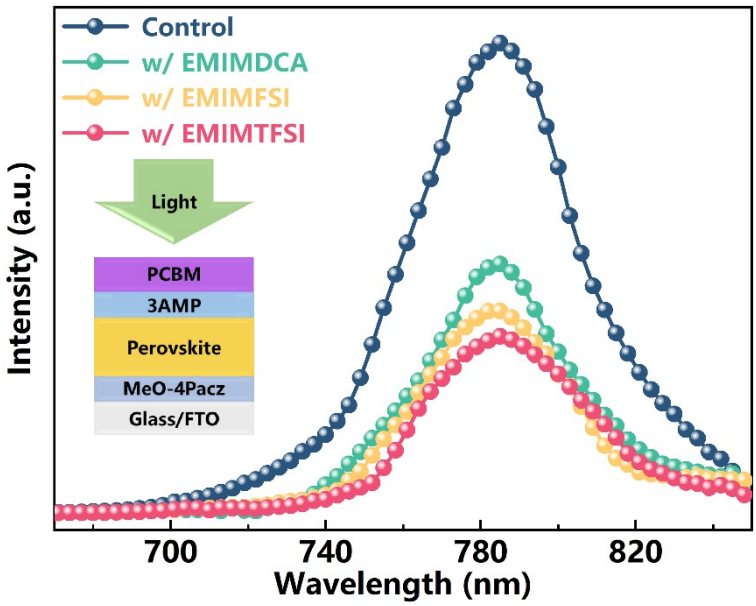

Figure S15. steady-state PL spectra for the device of Glass/FTO/Glass/FTO/MeO-4Pacz/Perovskite/3AMP/PCBM.

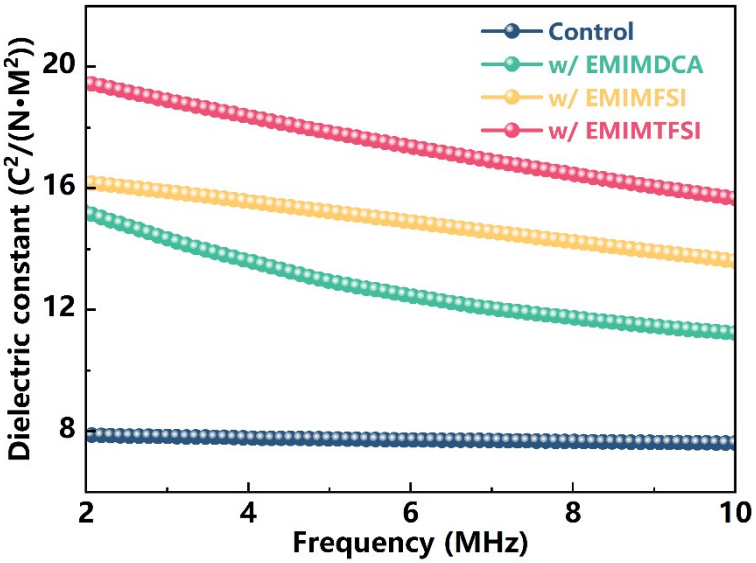

Figure S16. Dielectric constants of perovskite films with or without PH-IL optimization.

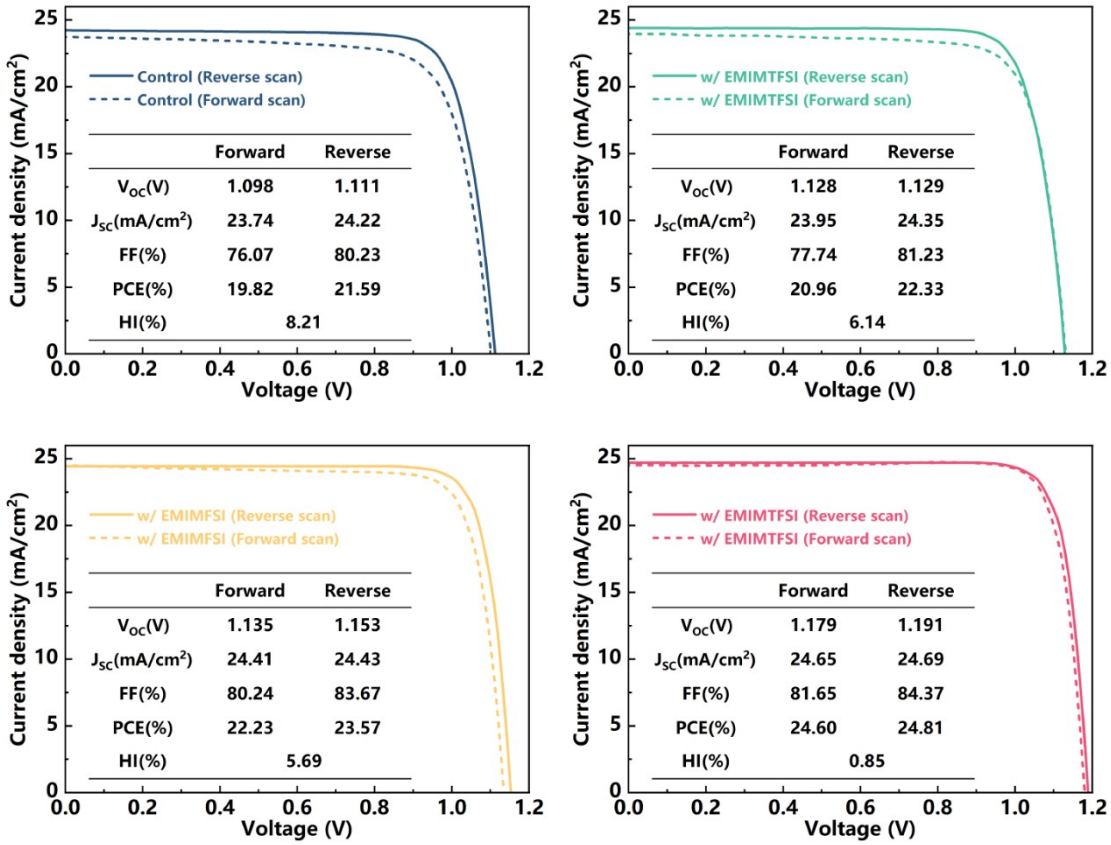

Figure S17. The negligible hysteresis effects of Control, w/EMIMDCA, w/EMIMFSI and w/EMIMTFSI.

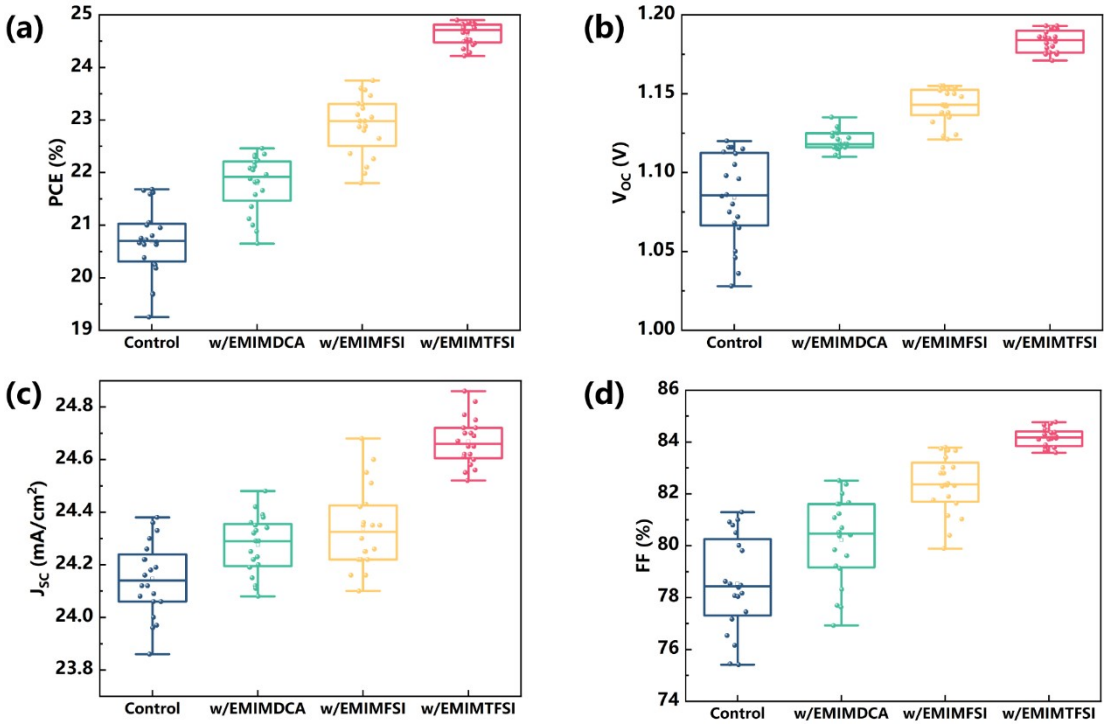

Figure S18. Statistics of the values of V_{OC}, J_{SC}, FF, and PCE from 20 devices of Control, w/EMIMDCA, w/EMIMFSI and w/EMIMTFSI.

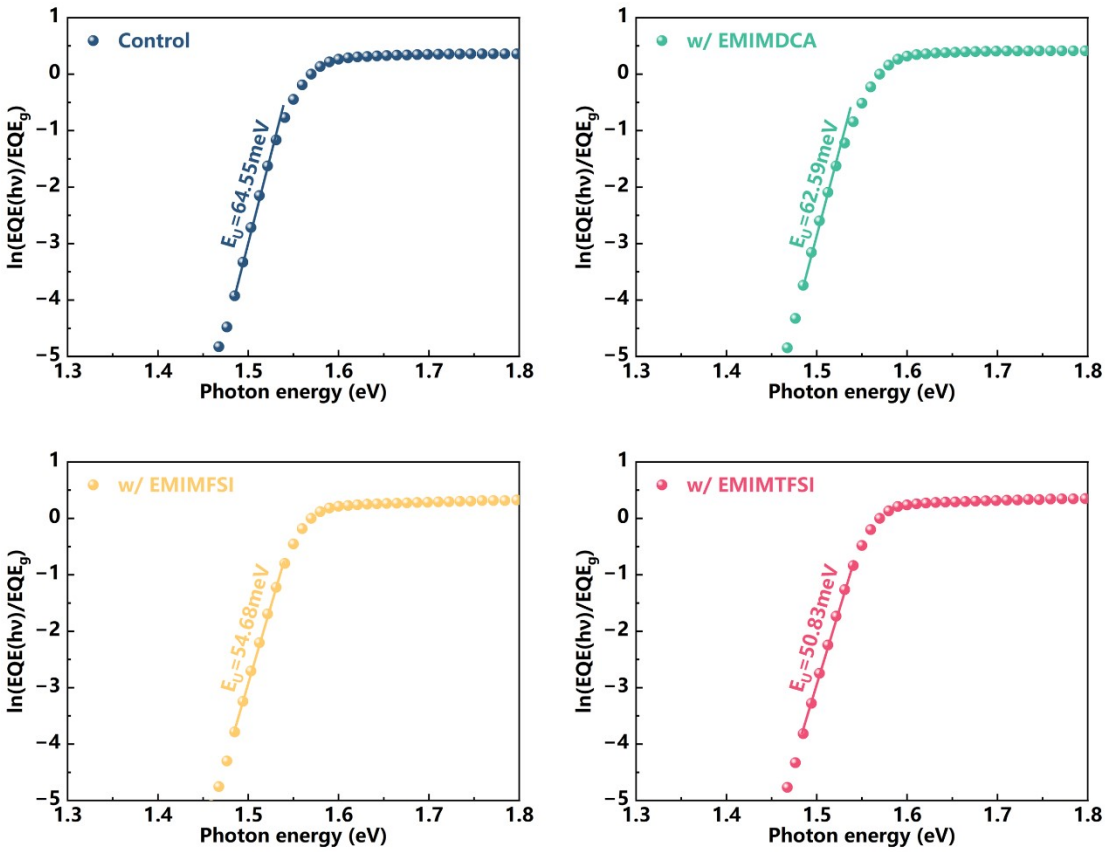

Figure S19. The Urbach energies of Control, w/EMIMDCA, w/EMIMFSI and w/EMIMTFSI.

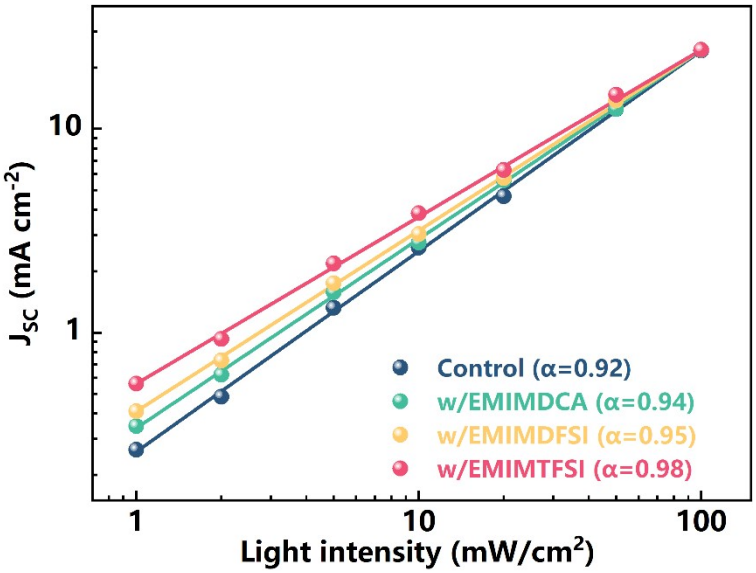

Figure S20. Light-intensity-dependent J_{SC} of perovskite films with or without PH-IL optimization.

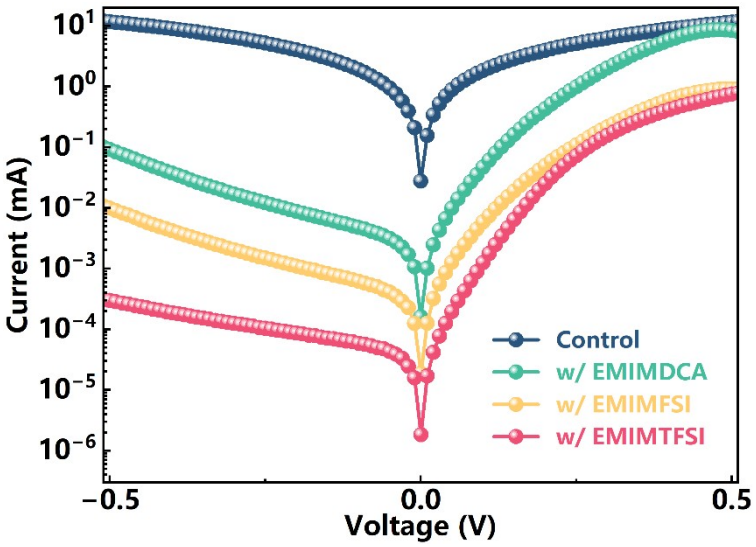

Figure S21. Dark J–V patterns of perovskite films with or without PH-IL optimization.

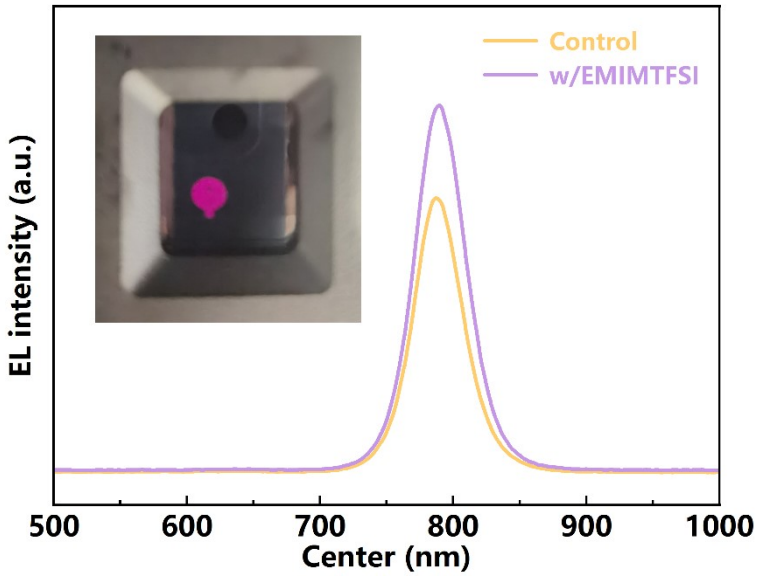

Figure S22. Electroluminescence (EL) spectrum of perovskite films with or without EMIMTFSI optimization.

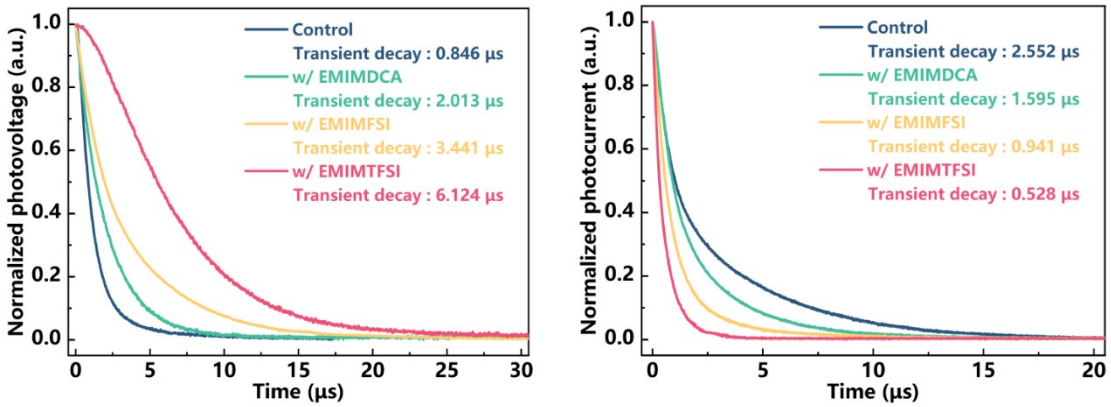

Figure S23. TPV and TPC patterns of perovskite films with or without PH-IL optimization.

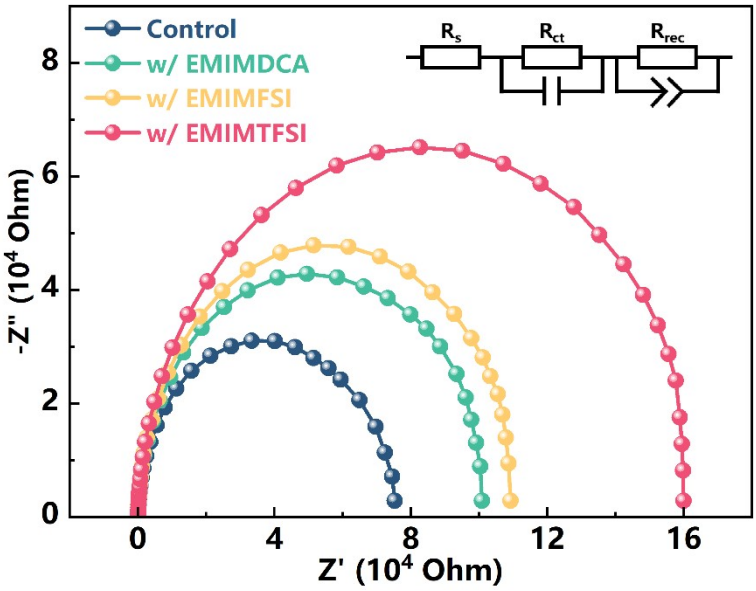

Figure S24. EIS pattern of perovskite films with or without PH-IL optimization.

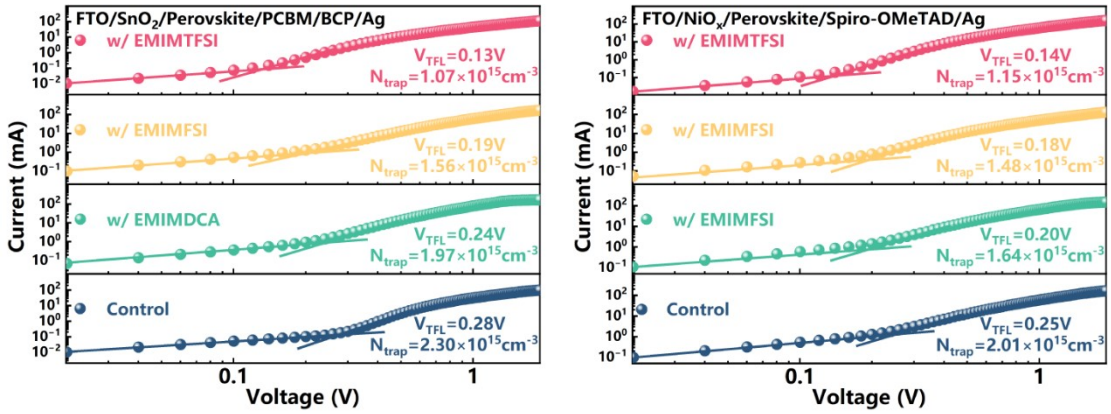

Figure S25. SCLC patterns (electron-only device and hole-only devices) of perovskite films with or without PH-IL optimization.

Experimental details:

Electron-only device: FTO/SnO_2/perovskite/PCBM/BCP/Ag

Hole-only device: FTO/MeO-4Pacz/perovskite/Spiro-OMeTAD/Ag

N_t in perovskite can be calculated as follows:

$$N_t = \frac{2\varepsilon\varepsilon_0 V_{TEL}}{eL^2}$$

where ε and ε_0 are the dielectric constant of perovskite film and vacuum, respectively, L is the thickness of perovskite film.

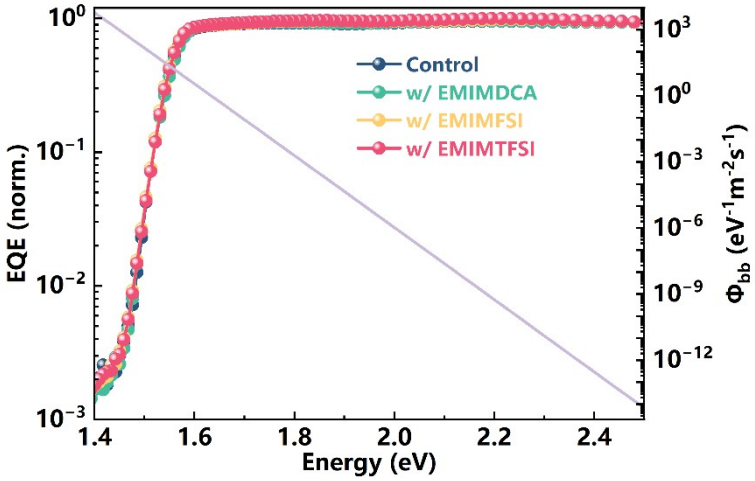

Figure S26. EQE spectrum and black body photon flux (purple line) for $J_{rad,0}$ in QFLS calculation.

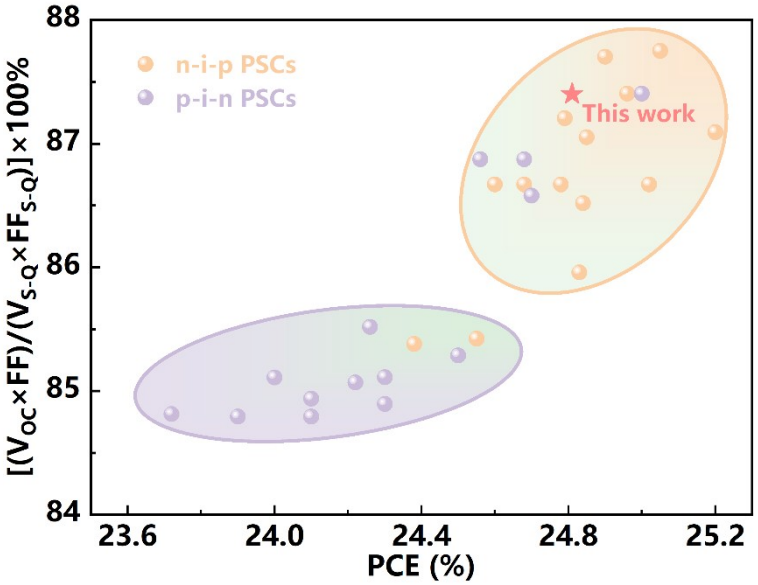

Figure S27. Comparison of V_{OC}×FF with S-Q limit of its corresponding band gap in literature.

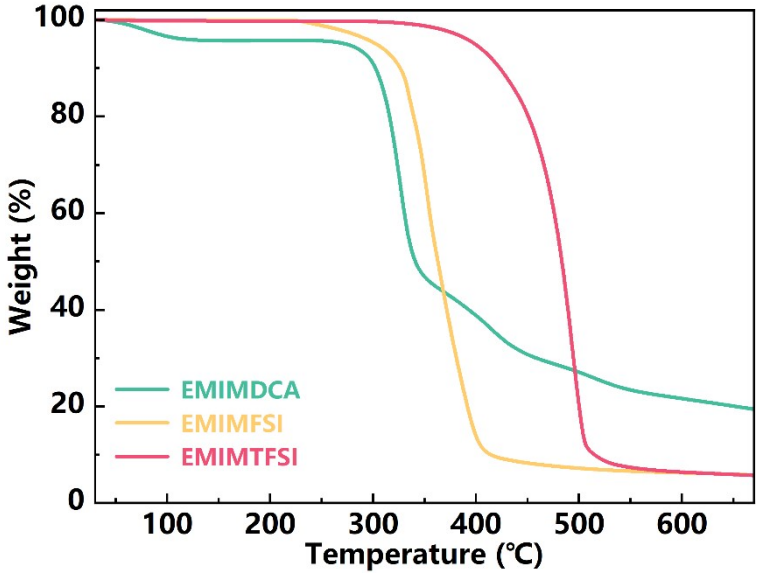

Figure S28. TGA pattern of EMIMDCA, EMIMFSI and EMIMTFSI.

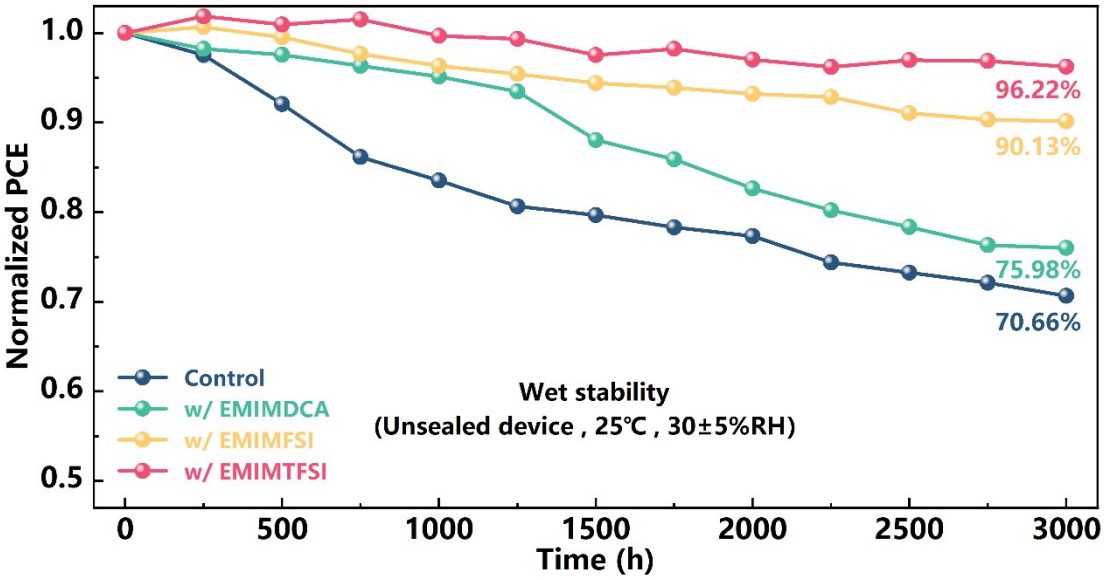

Figure S29. Wet stability of perovskite films placing in the ambient atmosphere (25 ± 5 ℃ and 30 ± 5%RH) for 3000 h.

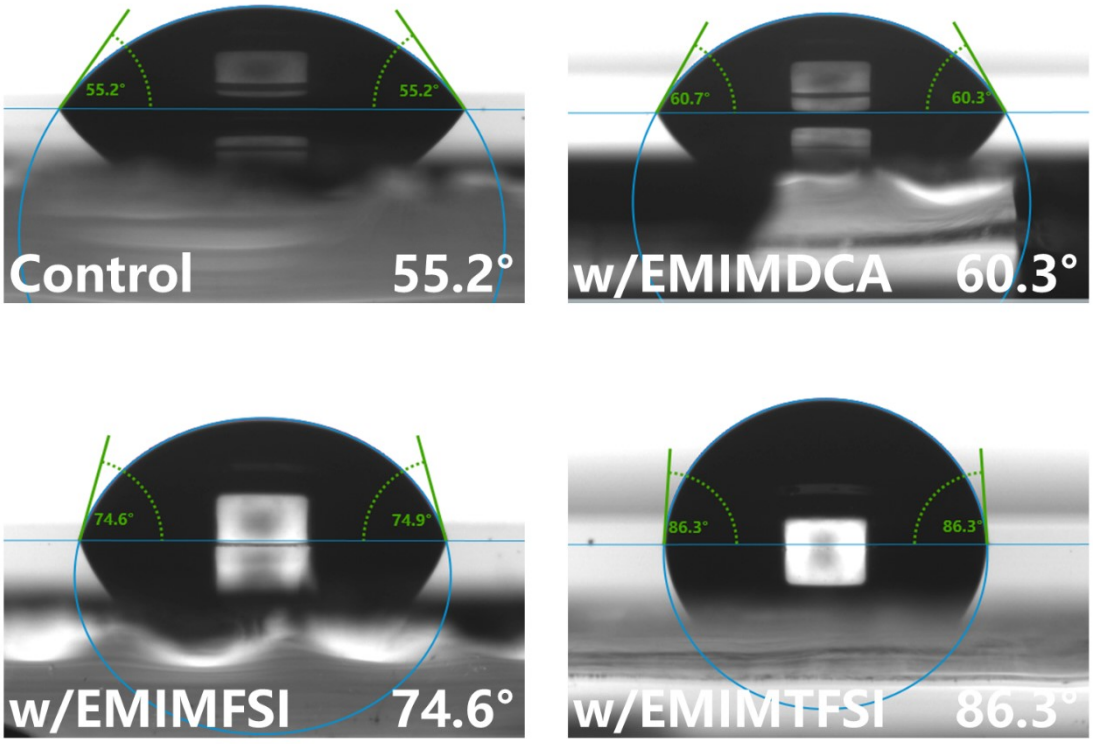

Figure S30. Water contact angles of Control, w/EMIMDCA, w/EMIMFSI and w/EMIMTFSI.

Table S1. Fitting parameters of the bi-exponential decay function in TRPL spectra of Control, w/EMIMDCA, w/EMIMFSI and w/EMIMTFSI.

Device	A_1(%)	τ_1(ns)	A_2(%)	τ_2(ns)	τ_{ave}(ns)
Control	69.94	106.36	30.06	896.41	343.82
w/EMIMDCA	56.06	44.95	43.94	1246.98	573.18
w/EMIMFSI	49.83	61.70	50.17	2773.55	1234.76
w/EMIMTFSI	49.61	127.94	50.39	3266.88	1709.69

Table S2. The detailed photovoltaic parameters of the champion device (Control, w/EMIMDCA, w/EMIMFSI and w/EMIMTFSI)

Device	V_{OC}(V)	J_{SC}(mA/cm^2)	FF(%)	PCE(%)
Control	1.111	24.22	80.23	21.59
w/EMIMDCA	1.129	24.35	81.23	22.33
w/EMIMFSI	1.153	24.43	83.67	23.57
w/EMIMTFSI	1.191	24.69	84.37	24.81

Table S3. The hysteresis effects of the champion device (Control, w/EMIMDCA, w/EMIMFSI and w/EMIMTFSI)

Device	Direction	V_{OC}(V)	J_{SC}(mA/cm²)	FF(%)	PCE(%)	HI(%)
Control	Reverse	1.111	24.22	80.23	21.59	8.20
	Forward	1.098	23.74	76.07	19.82	
w/EMIMDCA	Reverse	1.129	24.35	81.23	22.33	6.14
	Forward	1.128	23.95	77.44	20.96	
w/EMIMFSI	Reverse	1.153	24.43	83.69	23.57	5.69
	Forward	1.135	24.41	80.24	22.23	
w/EMIMTFSI	Reverse	1.191	24.69	84.37	24.81	0.85
	Forward	1.179	24.65	81.65	24.60	

Table S4. The calculated parameters relating to QFLS.

Device	J_G(mA/cm^2)	$J_{0,rad}$(A/m^2)	QLFS$_{rad}$(eV)	QLFS(eV)
Control	23.70	6.22×10^{-20}	1.286	1.174
w/EMIMDCA	23.78	5.96×10^{-20}	1.287	1.178
w/EMIMFSI	24.13	5.59×10^{-20}	1.289	1.188
w/EMIMTFSI	24.30	5.26×10^{-20}	1.291	1.199

Table S5. Performance comparison of p-i-n PSCs by IL optimization in recently reported.

IL	Perovskite components	V_{OC} (V)	J_{SC} (mA/cm²)	FF (%)	PCE (%)	Ref.
$BMPBF_4$	$Cs_{0.15}FA_{0.65}MA_{0.2}Pb(I_{0.9}Br_{0.1})_3$	1.16	19.50	77.00	17.30	[9]
$BMIMBF_4$	$MAPbI_3$	1.04	21.32	82.00	18.12	[10]
EMIMAE	$Cs_{0.05}FA_{0.85}MA_{0.1}Pb(I_{0.9}Br_{0.1})_3$	1.04	22.50	79.00	18.60	[11]
$BMIMBF_4$	$MAPbI_3$	1.06	23.52	77.00	19.30	[12]
$BMIMBF_4$	$Cs_{0.05}(FA_{0.83}MA_{0.17})_{0.95}Pb(I_{0.9}Br_{0.1})_3$	1.08	23.80	81.00	19.80	[13]
EMIMBr	$MAPbI_3$	1.11	23.74	75.90	20.00	[14]
EMIC	$MAPbI_3$	1.08	23.91	78.00	20.06	[15]
BAAc	$Cs_{0.05}(FA_{0.85}MA_{0.15})_{0.95}Pb(I_{0.9}Br_{0.1})_3$	1.12	22.70	79.00	20.10	[16]
$BMIMBF_4$	$Cs_{0.05}FA_{0.81}MA_{0.14}Pb(I_{0.9}Br_{0.1})_3$	1.11	22.45	82.52	20.31	[17]
$MAPF_6$	$Cs_{0.15}FA_{0.65}MA_{0.2}Pb(I_{0.8}Br_{0.2})_3$	1.19	21.11	81.87	20.64	[18]
PeImTFSI	$Cs_{0.05}(FA_{0.83}MA_{0.17})_{0.95}Pb(I_{0.83}Br_{0.17})_3$	1.16	22.54	81.93	21.39	[19]
$BMIMBF_4$	$Cs_{0.05}(FA_{0.85}MA_{0.15})_{0.95}Pb(I_{0.85}Br_{0.15})_3$	1.13	23.75	84.21	22.62	[20]
MAFa	$FAPbI_3$	1.16	25.06	82.80	24.08	[21]
BzMIMI	$Cs_{0.05}(FA_{0.92}MA_{0.08})_{0.95}Pb(I_{0.92}Br_{0.08})_3$	1.20	23.70	84.42	24.09	[22]
EMIMTFSI	**$Cs_{0.05}(FA_{0.92}MA_{0.08})_{0.95}Pb(I_{0.92}Br_{0.08})_3$**	**1.19**	**24.52**	**84.96**	**24.81**	**This work**

References

[1] C. T. Lee, W. T. Yang, R. G. Parr, *Phys. Rev. B* **1988**, *37*, 785.

[2] R. Krishnan, J. S. Binkley, R. Seeger, J. A. Pople, *J. Chem. Phys.* **1980**, *72*, 650.

[3] G. Kresse, D. Joubert, *Phys. Rev. B* **1999**, *59*, 1758.

[4] J. P. Perdew, K. Burke, M. Ernzerhof, *Phys. Rev. Lett.* **1996**, *77*, 3865.

[5] K. Zhang, A. Spaeth, O. Almora, V. M. Le Corre, J. Wortmann, J. Zhang, Z. Xie, A. Barabash, M. S. Hammer, T. Heumueller, J. Min, R. Fink, L. Lueer, N. Li, C. J. Brabec, *ACS Energy Lett.* **2022**, *7*, 3235.

[6] P. Caprioglio, J. A. Smith, R. D. J. Oliver, A. Dasgupta, S. Choudhary, M. D. Farrar, A. J. Ramadan, Y.-H. Lin, M. G. Christoforo, J. M. Ball, J. Diekmann, J. Thiesbrummel, K.-A. Zaininger, X. Shen, M. B. Johnston, D. Neher, M. Stolterfoht, H. J. Snaith, *Nature communications* **2023**, *14*, 932.

[7] W. Peng, K. Mao, F. Cai, H. Meng, Z. Zhu, T. Li, S. Yuan, Z. Xu, X. Feng, J. Xu, M. D. McGehee, J. Xu, *Science* **2023**, *379*, 683.

[8] M. A. Green, *Solar Cells* **1982**, *7*, 337.

[9] Y.-H. Lin, N. Sakai, P. Da, J. Wu, H. C. Sansom, A. J. Ramadan, S. Mahesh, J. Liu, R. D. J. Oliver, J. Lim, L. Aspitarte, K. Sharma, P. K. Madhu, A. B. Morales-Vilches, P. K. Nayak, S. Bai, F. Gao, C. R. M. Grovenor, M. B. Johnston, J. G. Labram, J. R. Durrant, J. M. Ball, B. Wenger, B. Stannowski, H. J. Snaith, *Science* **2020**, *369*, 96.

[10] X. Zheng, T. Jiang, L. Bai, X. Chen, Z. Chen, X. Xu, D. Song, X. Xu, B. Li, Y. Yang, *RSC Adv.* **2020**, *10*, 18400.

[11] Y. Li, J. Song, Y. Zhang, T. Kong, X. Liu, D. Bi, *J. Phys. Chem. Lett.* **2022**, *13*, 10597.

[12] M. Li, C. Zhao, Z.-K. Wang, C.-C. Zhang, H. K. H. Lee, A. Pockett, J. Barbe, W. C. Tsoi, Y.-G. Yang, M. J. Carnie, X.-Y. Gao, W.-X. Yang, J. R. Durrant, L.-S. Liao, S. M. Jain, *Adv. Energy Mater.* **2018**, *8*, 1801509.

[13] S. Bai, P. Da, C. Li, Z. Wang, Z. Yuan, F. Fu, M. Kawecki, X. Liu, N. Sakai, J. T.-W. Wang, S. Huettner, S. Buecheler, M. Fahlman, F. Gao, H. J. Snaith, *Nature* **2019**, *571*, 245.

[14] X. Zhuang, X. Chen, L. Xu, S. Liu, Y. Wu, Z. Shi, Q. Zhou, B. Li, H. Yan, P. Reiss, H. Song, *J Colloid Interface Sci* **2022**, *622*, 469.

[15] X. Zhou, M. Hu, C. Liu, L. Zhang, X. Zhong, X. Li, Y. Tian, C. Cheng, B. A. Xu, *Nano Energy* **2019**, *63*, 103866.

[16] J. Ran, H. Wang, W. Deng, H. Xie, Y. Gao, Y. Yuan, Y. Yang, Z. Ning, B. Yang, *Sol. RRL* **2022**, *6*, 2200176.

[17] L. A. Castriotta, E. Calabro, F. Di Giacomo, S. H. Reddy, D. Takhellambam, B. Paci, A. Generosi, L. Serenelli, F. Menchini, L. Martini, M. Tucci, A. Di Carlo, *Nano Energy* **2023**, *109*, 108268.

[18] J. Tao, X. Liu, J. Shen, S. Han, L. Guan, G. Fu, D.-B. Kuang, S. Yang, *Acs Nano* **2022**, *16*, 10798.

[19] P. Caprioglio, D. S. Cruz, S. Caicedo-Davila, F. Zu, A. A. Sutanto, F. Pena-Camargo, L. Kegelmann, D. Meggiolaro, L. Gregori, C. M. Wolff, B. Stiller, L. Perdigon-Toro, H. Koebler, B. Li, E. Gutierrez-Partida, I. Lauermann, A. Abate, N. Koch, F. De Angelis, B. Rech, G. Grancini, D. Abou-Ras, M. K. Nazeeruddin, M. Stolterfoht, S. Albrecht, M. Antonietti, D. Neher, *Energy Environ. Sci.* **2021**, *14*, 4508.

[20] S. Wang, Y. Li, J. Yang, T. Wang, B. Yang, Q. Cao, X. Pu, L. Etgar, J. Han, J. Zhao, X. Li, A. Hagfeldt, *Angew. Chem. Int. Ed.* **2022**, *61*, e202116534.
[21] X. Jiang, X. Wang, X. Wu, S. Zhang, B. Liu, D. Zhang, B. Li, P. Xiao, F. Xu, H. Lu, T. Chen, A. K. Y. Jen, S. Yang, Z. Zhu, *Adv. Energy Mater.* **2023**, *13*, 2300700.
[22] Y. Zhang, C. Li, E. Bi, T. Wang, P. Zhang, X. Yang, H. Chen, *Adv. Energy Mater.* **2022**, *12*, 2202191.